Preservation and destruction of the purity of two-photon states in the interaction with a classical nanoscatterer

Álvaro Nodar,[1,*] Ruben Esteban,[1,2] Carlos Maciel-Escudero,[1,3,†] Jon Lasa-Alonso,[1,2,‡] Javier Aizpurua,[1,2,4,5] and Gabriel Molina-Terriza[1,2,4,§]

[1]*Centro de Física de Materiales (CFM-MPC), CSIC-UPV/EHU, Paseo Manuel de Lardizabal 5, 20018 Donostia-San Sebastián, Spain*

[2]*Donostia International Physics Center (DIPC), Paseo Manuel de Lardizabal 4, 20018 Donostia-San Sebastián, Spain*

[3]*CIC NanoGUNE BRTA and Department of Electricity and Electronics, UPV/EHU, Tolosa Hiribidea 76, 20018 Donostia-San Sebastián, Spain*

[4]*IKERBASQUE, Basque Foundation for Science, María Díaz de Haro 3, 48013 Bilbao, Spain*

[5]*Department of Electricity and Electronics, University of the Basque Country (UPV/EHU), 48940 Leioa, Spain*

(Received 7 November 2022; accepted 21 December 2025; published 20 February 2026)

The optical resonances supported by nanostructures offer the possibility to enhance the interaction between matter and quantum states of light. On the other hand, due to abrupt changes in the optical response the quantum states of light can be significantly affected by the interaction. In this work, we provide a framework to study the scattering of quantum states of light (with information encoded in their helicity) by a nanostructure. We analyze the purity of the scattered output quantum state and find that the purity of the incident state can be lost when it interacts with the optical resonances of the nanostructure. To explain the loss of quantum purity, we develop a physical picture based on time delays and frequency shifts between the output two-photon modes. The framework and analysis proposed in this work establish a tool to address the interaction between quantum light and nanoenvironments.

DOI: 10.1103/hb1h-jw72

I. INTRODUCTION

Quantum entanglement is a fragile resource required for most quantum applications. There have been extensive studies to quantify and exploit the degree of entanglement of different systems, and also to analyze the loss of entanglement and purity through decoherence [1,2]. One of the benefits of encoding quantum information in optical states is that they are very resilient to decoherence, while at the same time, by their very nature, photons are excellent information carriers for quantum communication protocols [3–5]. However, photons do not interact strongly with material particles and structures, which limits the possibilities of processing photonic quantum information [6,7].

Several techniques are being developed in order to enhance photon interactions, such as quantum optomechanical systems, optical metamaterials, high-density gases, slow-light materials, and several others [5,8]. Among these, engineering nanophotonic nanostructures for quantum information processing offers the possibility, not only to enhance light-matter interactions, but also to manipulate light in devices with a footprint of the order of the wavelength. While the use of nanostructures and the study of their optical resonances to enhance the classical interaction of light and matter has a long tradition [9–12], to the best of our knowledge, a formal, detailed study of the effect of the interaction of quantum states of light with such nanostructures is missing.

In this work, we provide a framework to study the interaction between quantum states of light and a classical nanostructure, i.e., a nanoscatterer that can be described with classical constitutive equations. Our approach is general, although here we focus on an experimentally relevant situation: the scattering of two-photon states of light by a rotationally symmetric nanostructure. The symmetry of the problem allows us to focus on electromagnetic modes with well-defined total angular momentum $m = l + s$, where l and s represent the orbital and spin angular momentum, respectively. These types of quantum states are very robust to propagation [3,13,14] and can encode more information than, for example, polarization states by using several values of l [15–18]. Interestingly, they can be manipulated in a controlled manner with rotationally symmetric nanostructures that allow for the conservation of the total angular momentum m of the incoming light [19,20].

II. INPUT AND OUTPUT STATES

The theoretical framework used to describe the quantum scattering process is based on an input/output general

*Present address: Global Data Quantum, Alameda Rekalde 18, 7 izq., 48009 Bilbao, Bizkaia.

†Present address: Department of Physics, Philipps-Universität Marburg, 35032 Marburg, Germany.

‡Present address: Basic Sciences Department, Mondragon Unibertsitatea, Olagorta Kalea 26, 48014 Bilbao, Spain.

§Contact author: gabriel.molina@ehu.eus

Published by the American Physical Society under the terms of the Creative Commons Attribution 4.0 International license. Further distribution of this work must maintain attribution to the author(s) and the published article's title, journal citation, and DOI.

formalism [20–24]. We consider that the input and output states of the system are quantum states of light composed by two entangled photons, where the two photons have total angular momentum $m = 0$, and the information is encoded in their helicity Λ (defined as the projection of the spin on the direction of propagation), which takes $\Lambda = +1$ or $\Lambda = -1$ values [20]. Let us first consider a simpler case where the input two-photon states are monochromatic. While not experimentally achievable, this ideal case of monochromatic states facilitates the introduction of the input-output formalism used in this work. Specifically, we consider a basis of four input two-photon modes that completely describes any input monochromatic two-photon states:

$$|\psi^i_\pm(\omega_1,\omega_2)\rangle = \tfrac{1}{2}\{\hat{a}^\dagger_i(\omega_1)\hat{a}^\dagger_i(\omega_2) \pm \hat{b}^\dagger_i(\omega_1)\hat{b}^\dagger_i(\omega_2)\}|0\rangle, \quad (1a)$$

$$|\chi^i_\pm(\omega_1,\omega_2)\rangle = \tfrac{1}{2}\{\hat{a}^\dagger_i(\omega_1)\hat{b}^\dagger_i(\omega_2) \pm \hat{b}^\dagger_i(\omega_1)\hat{a}^\dagger_i(\omega_2)\}|0\rangle, \quad (1b)$$

where $|0\rangle$ is the vacuum state, and ω_1 and ω_2 are the frequencies of the two photons. The basis of the two-photon output monochromatic modes also has four elements, $|\psi^o_\pm(\omega_1,\omega_2)\rangle$ and $|\chi^o_\pm(\omega_1,\omega_2)\rangle$, which follow Eqs. (1a) and (1b), respectively, but the input "i" labels are substituted by the output "o" labels,

$$|\psi^o_\pm(\omega_1,\omega_2)\rangle = \tfrac{1}{2}\{\hat{a}^\dagger_o(\omega_1)\hat{a}^\dagger_o(\omega_2) \pm \hat{b}^\dagger_o(\omega_1)\hat{b}^\dagger_o(\omega_2)\}|0\rangle, \quad (2a)$$

$$|\chi^o_\pm(\omega_1,\omega_2)\rangle = \tfrac{1}{2}\{\hat{a}^\dagger_o(\omega_1)\hat{b}^\dagger_o(\omega_2) \pm \hat{b}^\dagger_o(\omega_1)\hat{a}^\dagger_o(\omega_2)\}|0\rangle. \quad (2b)$$

The modes of light are described by the input (output) $\hat{a}^\dagger_{i(o)}(\omega)$ and $\hat{b}^\dagger_{i(o)}(\omega)$ bosonic operators that indicate the creation of an input (output) photon with helicity $\Lambda = +1$ or $\Lambda = -1$, respectively. The $\hat{a}^\dagger_{i(o)}(\omega)$ and $\hat{b}^\dagger_{i(o)}(\omega)$ bosonic operators satisfy the canonical commutation relations [25] and operate on a single frequency ω.

Recent experiments have measured a degradation of input quantum states (quantified below by means of the loss of purity) after scattering off a nanostructure [20]. In particular, in these (and other similar) experiments [23,26], the incident photon pairs are generated in a superposition of states of different frequencies, typically by a standard spontaneous parametric down-conversion (SPDC) process. In this work, we analyze the mechanism by which the scattering of these nonmonochromatic states can result in a loss of purity. With this purpose, we analyze the scattering of states that are frequency superpositions of the monochromatic two-photon state $|\psi^i_+(\omega_1,\omega_2)\rangle$ as given by

$$|\Psi^i_+\rangle = \iint d\omega_1 d\omega_2 \phi(\omega_1,\omega_2)|\psi^i_+(\omega_1,\omega_2)\rangle. \quad (3)$$

where $\phi(\omega_1,\omega_2)$ is the two-photon spectral function that we approximate as the product of two Gaussian functions —both centered at the central frequency ω_{in} (or central wavelength $\lambda_{\text{in}} = 2\pi c/\omega_{\text{in}}$)—with variance $\sigma^2 = 9\,\text{THz}^2$, chosen to be similar to the one used in recent experiments [27,28] (for the considered spectral range this value corresponds to $\sigma_\lambda \approx 3.4\,\text{nm}$, see depiction of the pulse in Fig. 7).

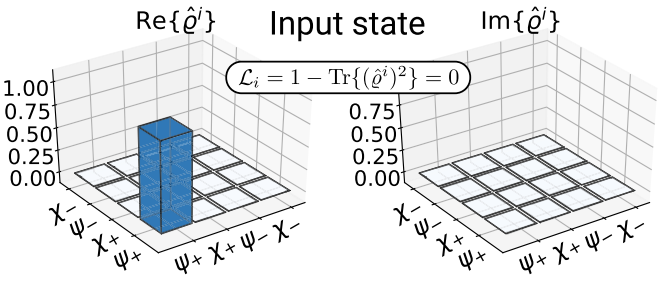


FIG. 1. Real (left) and imaginary (right) components of $\hat{\varrho}^i$, the density matrix associated with the input state $|\Psi^i_+\rangle$. The two-photon spectral function is centered at $\omega_{\text{in}} = 17.5 \times 10^{14}$ rad/s and has a variance of $\sigma^2 = 9\,\text{THz}^2$. $\mathcal{L}_i = 0$ indicates that the input state is pure.

Thus,

$$\phi(\omega_1,\omega_2) = \frac{1}{\sigma\sqrt{\pi}} \exp\left(-\frac{(\omega_1-\omega_{\text{in}})^2}{2\sigma^2}\right) \times \exp\left(-\frac{(\omega_2-\omega_{\text{in}})^2}{2\sigma^2}\right). \quad (4)$$

Note that this expression of $\phi(\omega_1,\omega_2)$ implies that the two input photons are indistinguishable, since $\phi(\omega_1,\omega_2) = \phi(\omega_2,\omega_1)$.

The scattering of the rest of the elements in the basis in Eq. (1) is studied in Sec. III E.

A. Experimentally accesible density matrix

In order to approach a realistic characterization of quantum-entangled states, we consider that the scattered states are measured through the postselection of two-photon states, where the scattered states with less than two photons are ignored. We also consider in the following that the detectors are "blind" to the frequency degree of freedom. The input and output quantum states are best described with the experimentally accessible postselected density matrix $\hat{\varrho}$ resulting from tracing out the frequency degree of freedom. Thus, the elements $\langle\xi|\hat{\varrho}|\xi'\rangle$ of the density matrix correspond to the results of standard quantum state tomography measurements [25,29],

$$\langle\xi|\hat{\varrho}^{i(o)}|\xi'\rangle = \mathcal{K}\iint \langle\xi^{i(o)}(\omega_1,\omega_2)|\Psi^{i(o)}_+\rangle \times \langle\Psi^{i(o)}_+|\xi'^{i(o)}(\omega_1,\omega_2)\rangle d\omega_1 d\omega_2, \quad (5)$$

where $\mathcal{K}$ is a normalization constant that ensures $\text{Tr}\{\hat{\varrho}^{i(o)}\} = 1$. $|\xi^{i(o)}(\omega_1,\omega_2)\rangle$ and $|\xi'^{i(o)}(\omega_1,\omega_2)\rangle$ can be any superposition of the $|\psi^{i(o)}_\pm(\omega_1,\omega_2)\rangle$ and $|\chi^{i(o)}_\pm(\omega_1,\omega_2)\rangle$ states given in Eqs. (1) and (2). For example, Fig. 1 shows the density matrix $\hat{\varrho}^i$ of the incident state $|\Psi^i_+\rangle$ [Eq. (3)] calculated using Eq. (5). In this case, $\hat{\varrho}^i$ is characterized by a single nonzero element corresponding to $\langle\psi_+|\hat{\varrho}^i|\psi_+\rangle$, and there is no contribution from the other elements of the basis [Eqs. (1a) and (1b)]. The loss of purity for any quantum state can then be quantified using

$$\mathcal{L}_{i(o)} = 1 - \text{Tr}\{(\hat{\varrho}^{i(o)})^2\}, \quad (6)$$

where $\mathcal{L}_{i(o)} = 0$ indicates a pure state and $\mathcal{L}_{i(o)} > 0$ a mixed state. For the two-photon state under consideration, where

there are four possible orthogonal states, a maximally mixed state would have only elements in the diagonal with the same value, i.e., $\hat{\varrho}^{i(o)} = \mathrm{diag}(1/4, 1/4, 1/4, 1/4)$. Therefore, the maximum value attainable for the loss of purity is $\mathcal{L}_{i(o)} = 3/4$. The input density matrix $\hat{\varrho}^i$ in Fig. 1 satisfies $\mathcal{L}_i = 1 - \mathrm{Tr}\{(\hat{\varrho}^i)^2\} = 0$, which confirms that $\hat{\varrho}^i$ is a pure state [25].

III. QUANTUM TRANSFORMATION

We next discuss how to analyze the loss of purity due to the scattering (in the linear regime) of $m = 0$ photons by a rotationally symmetric nanostructure. Rotationally symmetric structures conserve the total angular momentum of the incident light. However, the conservation of the total angular momentum m does not imply the conservation of the vectorial degree of freedom of light, which is determined by the helicity Λ. Since the states of light studied in this work are determined by m and Λ, the input electromagnetic modes with $m = 0$ and $\Lambda = +1$ (or $\Lambda = -1$) can only be scattered into two different output electromagnetic modes with $m = 0$ (due to m conservation) and $\Lambda = +1$ or $\Lambda = -1$. Further, we consider that photons can be lost or dissipated in the scattering process. This situation, where two input electromagnetic modes are either lost or transformed into two other output electromagnetic modes, is analogous to the situation produced in a lossy beam splitter [21–23]. Thus, we can directly adapt the transformation of lossy beam splitters to our system, resulting in the following equations connecting the output and input annihilation operators:

$$\begin{aligned}\hat{a}_o(\omega) &= \alpha_{+1}(\omega)\hat{a}_i(\omega) + \beta_{+1}(\omega)\hat{b}_i(\omega) + \hat{L}_{+1}(\omega),\\ \hat{b}_o(\omega) &= \alpha_{-1}(\omega)\hat{b}_i(\omega) + \beta_{-1}(\omega)\hat{a}_i(\omega) + \hat{L}_{-1}(\omega),\end{aligned} \tag{7}$$

where α_{+1}, α_{-1}, β_{+1}, and β_{-1} are the helicity-splitting coefficients that are fully described in the next subsection and that are calculated including all losses in the system (due to absorption and because the detectors do not capture all scattered photons). $\hat{L}_{+1}$ and $\hat{L}_{-1}$ are the Langevin operators that need to be included in the presence of losses so that the commutation relationships are conserved [22,30,31]. In this way, losses are fully accounted for in the lossy beam-splitter formalism, avoiding the challenges that ensue from the direct quantization of the response of a multimode nanoscatterer.

To briefly illustrate how to use Eq. (7) and obtain the output state scattered by a nanoparticle for a given input state, let us consider an example of a monochromatic input single photon state with $m = 0$ and $\Lambda = +1$ at frequency ω. Using the creation operator formalism, we write this input state as $|\psi_+^{i,1}\rangle = \hat{a}_i^\dagger(\omega)|0\rangle$. We obtain the output state (with one photon) by projecting the input state into the output single photon basis, i.e., we evaluate

$$\begin{aligned}&[|\psi_+^{o,1}\rangle\langle\psi_+^{o,1}| + |\psi_-^{o,1}\rangle\langle\psi_-^{o,1}|]|\psi_+^{i,1}\rangle\\ &\quad= [\hat{a}_o^\dagger(\omega)|0\rangle\langle 0|\hat{a}_o(\omega) + \hat{b}_o^\dagger(\omega)|0\rangle\langle 0|\hat{b}_o(\omega)]|\psi_+^i\rangle,\end{aligned} \tag{8}$$

where $|\psi_+^{o,1}\rangle = \hat{a}_o^\dagger(\omega)|0\rangle$ is the single photon output state with $m = 0$ and $\Lambda = +1$ at frequency ω. In the same way, $|\psi_-^{o,1}\rangle = \hat{b}_o^\dagger(\omega)|0\rangle$ is the single photon output state with $m = 0$ and $\Lambda = -1$, at frequency ω.

We simplify Eq. (8) by using Eq. (7), the standard commutation relations between the creation and annihilation operators, and considering the vanishing average of the Langevin operators ($\langle\hat{L}_{+1}\rangle = \langle\hat{L}_{-1}\rangle = 0$) [22]. $|\psi_+^i\rangle$ is then transformed to the output state:

$$|\psi_+^i\rangle \to \alpha_{+1}(\omega)\hat{a}_o^\dagger(\omega)|0\rangle + \beta_{-1}(\omega)\hat{b}_o^\dagger(\omega)|0\rangle. \tag{9}$$

A. Helicity-splitting coefficients

Equation (7) describes the scattering of quantum states of light, but α_{+1}, α_{-1}, β_{+1}, and β_{-1} coefficients can be calculated from the classical response of the system as obtained from Maxwell's equations because Maxwell's equations determine how the electromagnetic modes get transformed, both in the classical and quantum regimes [32,33]. We emphasize that in this work we are using a quantum description of the incident light and a classical description for the response of the nanoparticle. The classical description can be used whenever we deal with bulk systems in contraposition with systems with significant nonlinearities or that need a quantum description, such as single atomic samples. This work focuses on solid-state systems that can be described with an index of refraction. Thus, to obtain the helicity-splitting coefficients, we consider a classical scattering problem where incident light beam with $m = 0$ is scattered by the nanostructure. The scattered light is collected by a lens and then separated by its helicity contributions. Each helicity contribution is detected separately. For example, in this work, the detection is done by coupling each helicity contribution of the collected field to a single-mode fiber connected to a detector.

In particular, we consider two classical focused input beams with a helicity of either $\Lambda = +1$ or $\Lambda = -1$ and total angular momentum $m = 0$. The electric fields for these input beams are represented by $\boldsymbol{E}_{+1}^i$ and $\boldsymbol{E}_{-1}^i$, respectively. We then calculate the scattered fields $\boldsymbol{E}^{s(+1)}$ ($\boldsymbol{E}^{s(-1)}$), when the nanostructure is illuminated by the input beam, $\boldsymbol{E}_{+1}^i$ ($\boldsymbol{E}_{-1}^i$). The helicity-splitting coefficients are determined by projecting the scattered field into two classical output beams, $\boldsymbol{E}_{+1}^o$ and $\boldsymbol{E}_{-1}^o$, which also have an angular momentum of $m = 0$ and a helicity of $\Lambda = +1$ and $\Lambda = -1$, respectively,

$$\begin{aligned}\alpha_{+1}(\omega) &= \iint_{\mathcal{A}} d\mathcal{A}\big[\boldsymbol{E}_{+1}^o(\boldsymbol{r},\omega)\big]^* \cdot \boldsymbol{E}^{s(+1)}(\boldsymbol{r},\omega),\\ \alpha_{-1}(\omega) &= \iint_{\mathcal{A}} d\mathcal{A}\big[\boldsymbol{E}_{-1}^o(\boldsymbol{r},\omega)\big]^* \cdot \boldsymbol{E}^{s(-1)}(\boldsymbol{r},\omega),\\ \beta_{+1}(\omega) &= \iint_{\mathcal{A}} d\mathcal{A}\big[\boldsymbol{E}_{-1}^o(\boldsymbol{r},\omega)\big]^* \cdot \boldsymbol{E}^{s(+1)}(\boldsymbol{r},\omega),\\ \beta_{-1}(\omega) &= \iint_{\mathcal{A}} d\mathcal{A}\big[\boldsymbol{E}_{+1}^o(\boldsymbol{r},\omega)\big]^* \cdot \boldsymbol{E}^{s(-1)}(\boldsymbol{r},\omega).\end{aligned} \tag{10}$$

This operation corresponds to calculating the coupling between the fields collected by the lens and a system to project into the corresponding spatial and polarization modes. Specifically, we are considering a system with mode-shaping, single-mode fibers, and polarizers to select the modes for each helicity contribution. $\mathcal{A}$ is the surface of the aperture of the lens (which we consider identical to the area of the fiber). The modes selected for each projection correspond to $\boldsymbol{E}_{+1}^o$ and $\boldsymbol{E}_{-1}^o$.

In this work, we consider a mirror symmetric detection scheme (discussed in Sec. IV) such that $\alpha_{+1}(\omega) = \alpha_{-1}(\omega) = \alpha(\omega)$ and $\beta_{+1}(\omega) = \beta_{-1}(\omega) = \beta(\omega)$. In this case, Eq. (7) simplifies to

$$\hat{a}_o(\omega) = \alpha(\omega)\hat{a}_i(\omega) + \beta(\omega)\hat{b}_i(\omega) + \hat{L}_{+1}(\omega),$$
$$\hat{b}_o(\omega) = \alpha(\omega)\hat{b}_i(\omega) + \beta(\omega)\hat{a}_i(\omega) + \hat{L}_{-1}(\omega). \quad (11)$$

Note that, as the lens does not capture all emitted photons, $|\alpha(\omega)|^2 + |\beta(\omega)|^2 \leqslant 1$ even in the absence of absorption losses.

B. Output $|\Psi_+^o\rangle$ state

By considering the simplified transformation in Eq. (11), we can obtain the output state $|\Psi_+^o\rangle$ from the projection of the input state $|\Psi_+^i\rangle$, on all the two-photon states of the output basis:

$$|\Psi_+^o\rangle = \iint [|\psi_+^o(\omega_3,\omega_4)\rangle\langle\psi_+^o(\omega_3,\omega_4)| + |\psi_-^o(\omega_3,\omega_4)\rangle\langle\psi_-^o(\omega_3,\omega_4)| + |\chi_+^o(\omega_3,\omega_4)\rangle\langle\chi_+^o(\omega_3,\omega_4)| + |\chi_-^o(\omega_3,\omega_4)\rangle\langle\chi_-^o(\omega_3,\omega_4)|]d\omega_3 d\omega_4 \cdot \iint \phi(\omega_1,\omega_2)|\psi_+^i(\omega_1,\omega_2)\rangle d\omega_1 d\omega_2. \quad (12)$$

To evaluate Eq. (12), we first substitute the expressions of $\hat{a}_o(\omega)$ and $\hat{b}_o(\omega)$ operators in Eq. (11) into the expressions of $\langle\psi_+^o(\omega_1,\omega_2)|$, $\langle\psi_-^o(\omega_1,\omega_2)|$, $\langle\chi_+^o(\omega_1,\omega_2)|$, and $\langle\chi_-^o(\omega_1,\omega_2)|$ in Eqs. (2a) and (2b); i.e., we express the output basis bra states in terms of the input operators. Then, we perform the projection of each output bra state onto the $|\psi_+^i(\omega_1,\omega_2)\rangle$ state. After some algebraic manipulation, Eq. (12) becomes

$$|\Psi_+^o\rangle = \iint \phi(\omega_1,\omega_2)[C_\psi(\omega_1,\omega_2)|\psi_+^o(\omega_1,\omega_2)\rangle + C_\chi(\omega_1,\omega_2)|\chi_+^o(\omega_1,\omega_2)\rangle]d\omega_1 d\omega_2, \quad (13)$$

with $C_\psi(\omega_1,\omega_2)$ and $C_\chi(\omega_1,\omega_2)$ defined as

$$C_\psi(\omega_1,\omega_2) = \alpha(\omega_1)\alpha(\omega_2) + \beta(\omega_1)\beta(\omega_2), \quad (14a)$$

$$C_\chi(\omega_1,\omega_2) = \alpha(\omega_1)\beta(\omega_2) + \beta(\omega_1)\alpha(\omega_2). \quad (14b)$$

Equation (13) shows that, in general, the output state is a superposition of the double integral over two different entangled photon modes, $|\psi_+^o(\omega_1,\omega_2)\rangle$ and $|\chi_+^o(\omega_1,\omega_2)\rangle$. Each of these modes has a different amplitude, $C_\psi(\omega_1,\omega_2)\phi(\omega_1,\omega_2)$ for $|\psi_+^o(\omega_1,\omega_2)\rangle$ and $C_\chi(\omega_1,\omega_2)\phi(\omega_1,\omega_2)$ for $|\chi_+^o(\omega_1,\omega_2)\rangle$, as we systematically show in the scheme of Fig. 2. $C_\psi(\omega_1,\omega_2)$ and $C_\chi(\omega_1,\omega_2)$ coefficients in Eqs. (14a) and (14b) may have a strong frequency dependence due to rapid spectral changes of α and β coefficients, greatly affecting the purity of the output state. To illustrate the formalism, we artificially set $\beta(\omega) = 0.2$ and $\alpha(\omega) = \omega_L\gamma/[2(\omega_L^2 - \omega^2 + i\gamma\omega)]$ a Lorentzian function that mimics the resonant behavior of a nanostructure (where ω_L and γ are the central frequency and losses of the Lorentzian resonance, respectively). Figure 3 shows the output density matrix $\hat{\varrho}^o$ calculated using Eqs. (5) and (13)–(14b), for these α and β helicity-splitting coefficients and the incident pulsed illumination described in Eq. (4). The $\hat{\varrho}^o$ obtained for the output state represents a partially coherent superposition of $|\psi_+^o(\omega_1,\omega_2)\rangle$ and $|\chi_+^o(\omega_1,\omega_2)\rangle$ [as indicated by Eq. (13)]. The purity of this state is $\mathcal{L}_o \approx 0.4 > 0$ (i.e., the output state is mixed). Thus, this simple example demonstrates that the purity of the incident quantum state can be lost in the interaction with a resonant nanostructure.

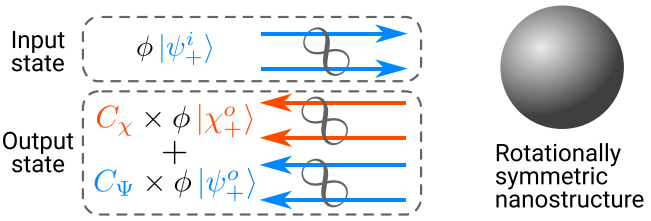


FIG. 2. Scheme of the scattering process. The $|\Psi_+^i\rangle$ input state is scattered by a rotationally symmetric nanostructure as a superposition of $|\psi_+^o\rangle$ and $|\chi_+^o\rangle$ with amplitudes given by $C_\psi\phi$ and $C_\chi\phi$, respectively.

C. Origin of the loss of purity under the quasimonochromatic approximation

To identify the origin of this loss of purity, we consider that the input two-photon spectral function, $\phi(\omega_1,\omega_2)$ is quasimonochromatic (i.e., its spectral variance σ^2 is significantly smaller than the central frequency of the pulse, ω_{in}). This approximation enables us to derive expressions for the terms $\phi(\omega_1,\omega_2)C_\psi(\omega_1,\omega_2)$ and $\phi(\omega_1,\omega_2)C_\chi(\omega_1,\omega_2)$ in Eq. (13), providing insight into the output scattered state.

Under the quasimonochromatic approximation, we first expand the α and β coefficients to first order around the central frequency of the two-photon spectral function ω_{in}:

$$\alpha(\omega) \approx A\left(1 + \frac{A'}{A}\Delta\omega\right), \quad (15)$$

$$\beta(\omega) \approx B\left(1 + \frac{B'}{B}\Delta\omega\right), \quad (16)$$

with $A = \alpha(\omega_{\text{in}})$, $B = \beta(\omega_{\text{in}})$, $A' = d\alpha(\omega)/d\omega|_{\omega_{\text{in}}}$, $B' = d\beta(\omega)/d\omega|_{\omega_{\text{in}}}$, and $\Delta\omega = \omega - \omega_{\text{in}}$.

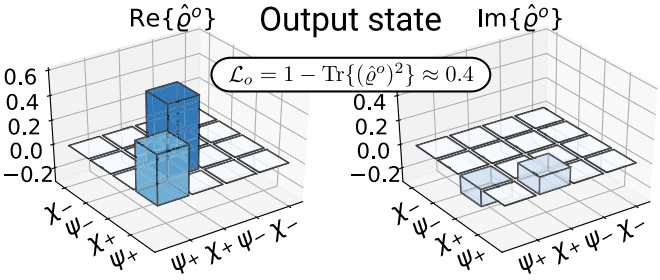


FIG. 3. Real (left) and imaginary (right) components of $\hat{\varrho}^o$, the postselected density matrix of the output state $|\Psi_+^o\rangle$ that results from the scattering of the incident input pulsed state $|\Psi_+^i\rangle$ in Fig. 1. For the calculation, we chose that the helicity-splitting coefficient $\beta(\omega) = 0.2$, and $\alpha(\omega)$ is a Lorentzian function with $\omega_L = 17.5 \times 10^{14}$ rad/s and $\gamma = 1$ THz. $\mathcal{L}_o \approx 0.4 > 0$ indicates that the output state is not pure.

Using Eqs. (15) and (16), we can write Eqs. (14a) and (14b) as

$$C_\psi(\omega_1,\omega_2) \approx (A^2+B^2)[1+(\Delta\omega_1+\Delta\omega_2)(F_\psi+i\tau_\psi)], \tag{17}$$

$$C_\chi(\omega_1,\omega_2) \approx 2AB[1+(\Delta\omega_1+\Delta\omega_2)(F_\chi+i\tau_\chi)], \tag{18}$$

with

$$F_\psi = \frac{1}{|A|^4+|B|^4+2|A|^2|B|^2\cos(2\delta)}\left\{\left(\frac{|A|'}{|A|}|A|^4+\frac{|B|'}{|B|}|B|^4\right) + |A|^2|B|^2\left[\cos(2\delta)\left(\frac{|A|'}{|A|}+\frac{|B|'}{|B|}\right)+\sin(2\delta)(\arg\{A\}'-\arg\{B\}')\right]\right\}, \tag{19}$$

$$\tau_\psi = \frac{1}{|A|^4+|B|^4+2|A|^2|B|^2\cos(2\delta)}\left\{\arg\{A\}'|A|^4+\arg\{B\}'|B|^4 + |A|^2|B|^2\left[\cos(2\delta)\left(\arg\{A\}'+\arg\{B\}'\right)+\sin(2\delta)\left(\frac{|B|'}{|B|}-\frac{|A|'}{|A|}\right)\right]\right\}, \tag{20}$$

$$F_\chi = \frac{1}{2}\left(\frac{|A|'}{|A|}+\frac{|B|'}{|B|}\right), \tag{21}$$

$$\tau_\chi = \frac{1}{2}(\arg\{A\}'+\arg\{B\}'). \tag{22}$$

In Eqs. (19)–(22), we have introduced $\arg\{A\}' = d\arg\{\alpha(\omega)\}/d\omega|_{\omega_{\rm in}}$, $\arg\{B\}' = d\arg\{\beta(\omega)\}/d\omega|_{\omega_{\rm in}}$, $\delta = \arg\{B\}-\arg\{A\}$, $|A|' = d|\alpha(\omega)|/d\omega|_{\omega_{\rm in}}$, and $|B|' = d|\beta(\omega)|/d\omega|_{\omega_{\rm in}}$. We further make the approximation $1+x\Delta\omega \approx e^{x\Delta\omega}$ in Eqs. (17) and (18), which gives

$$C_\psi(\omega_1,\omega_2) \approx (A^2+B^2)\exp[(\Delta\omega_1+\Delta\omega_2)(F_\psi+i\tau_\psi)], \tag{23}$$

$$C_\chi(\omega_1,\omega_2) \approx 2AB\exp[(\Delta\omega_1+\Delta\omega_2)(F_\chi+i\tau_\chi)]. \tag{24}$$

Then, the terms in Eq. (13) result in

$$\phi(\omega_1,\omega_2)C_\psi(\omega_1,\omega_2) \approx A_\psi\exp\left[-\frac{[\omega_1-(\omega_{\rm in}+\sigma^2F_\Psi)]^2}{2\sigma^2}+i\omega_1\tau_\psi\right] \times\exp\left[-\frac{[\omega_2-(\omega_{\rm in}+\sigma^2F_\Psi)]^2}{2\sigma^2}+i\omega_2\tau_\psi\right], \tag{25}$$

$$\phi(\omega_1,\omega_2)C_\chi(\omega_1,\omega_2) \approx A_\chi\exp\left[-\frac{[\omega_1-(\omega_{\rm in}+\sigma^2F_\chi)]^2}{2\sigma^2}+i\omega_1\tau_\chi\right] \times\exp\left[-\frac{[\omega_2-(\omega_{\rm in}+\sigma^2F_\chi)]^2}{2\sigma^2}+i\omega_2\tau_\chi\right], \tag{26}$$

with

$$A_\psi = \frac{1}{\sigma\sqrt{\pi}}(A^2+B^2)e^{F_\psi^2-i2\omega_{\rm in}\tau_\psi} \tag{27}$$

and

$$A_\chi = \frac{2}{\sigma\sqrt{\pi}}ABe^{F_\chi^2-i2\omega_{\rm in}\tau_\chi}. \tag{28}$$

Note that in Eqs. (19)–(28), A_Ψ, F_Ψ, τ_Ψ, A_χ, F_χ, and τ_χ depend only on the classical response of the system evaluated at the central frequency of the incident pulse, $\omega_{\rm in}$.

Equations (13), (25), and (26) show that the output two-photon modes can be represented as two distinct and superposed two-photon pulses, one associated with the $|\psi_+^o(\omega_1,\omega_2)\rangle$ states, and the other with the $|\chi_+^o(\omega_1,\omega_2)\rangle$ states. Each two-photon pulse can be factorized as two Gaussian pulses, one for each photon. However, the pulses associated with the $|\psi_+^o(\omega_1,\omega_2)\rangle$ and $|\chi_+^o(\omega_1,\omega_2)\rangle$ states have different properties. The pulse in Eq. (25) has an amplitude A_ψ, a common central frequency for both photons ($\omega_{\rm in}+\sigma^2F_\psi$), and a central time delay τ_ψ [identified from the $i\omega_1\tau_\psi$ and $i\omega_2\tau_\psi$ terms in Eq. (25)]. Figure 4 shows a scheme of this delay and frequency shift for one of the photons of the $|\psi_+^o(\omega_1,\omega_2)\rangle$ component of the output state.

Similarly, the pulse in Eq. (26) has an amplitude A_χ, a central frequency ($\omega_{\rm in}+\sigma^2F_\chi$), and a central time delay τ_χ.

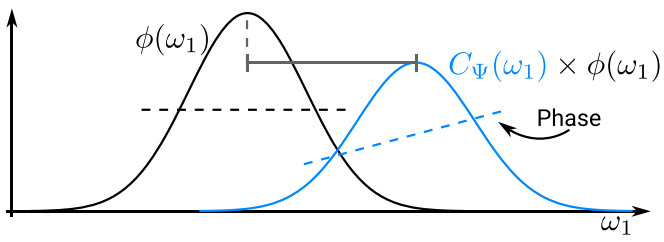


FIG. 4. Sketch of the effect of the interaction of the scatterer with the photon pulse shape. The black curve represents a typical Gaussian profile of the frequency of one of the photons (we represent this for simplicity, while in the text we consider a separable state in frequency for the biphoton wavefunction). After linearization of the parameters, the overall effect of the interaction with the particle on the photon state would be that the state is converted to another Gaussian profile (blue), which is frequency displaced with respect to the first one by a frequency σ^2F_Ψ, has a different amplitude, and its dephased by $\omega_1\tau_\Psi$ (indicated by a ramp in the phase of the frequency profile).

This implies that after the interaction with the nanostructure, the resulting quantum state is a superposition of two different quantum states with different time-frequency properties. As we show next, the loss of purity in the output state can be attributed to the difference in time delay and frequency shift between the output pulses.

D. Analytical expression of the loss of purity

Using Eqs. (5), (6), (13), (25), and (26), we obtain an analytical expression for the purity of the output state in the quasimonochromatic approximation,

$$\mathcal{L}_o = \frac{2|A_\Psi|^2|A_\chi|^2 e^{\sigma^2(F_\chi^2+F_\Psi^2)}}{\left(|A_\Psi|^2 e^{2\sigma^2 F_\Psi^2} + |A_\chi|^2 e^{2\sigma^2 F_\chi^2}\right)^2}\left[e^{\sigma^2\Delta F^2} - e^{-\sigma^2\Delta\tau^2}\right], \tag{29}$$

with $\Delta F = F_\Psi - F_\chi$ and $\Delta\tau = \tau_\Psi - \tau_\chi$. This equation indicates that the output state is pure under any of the following conditions:

(1) If $\sigma = 0$, corresponding to a purely monochromatic incident state. In this case, the output state is pure and consists of a superposition of two different states with amplitudes A_Ψ and A_χ [Eqs. (13), (25), (26)].

(2) If $\beta(\omega) = 0$ (within the spectral width of the incident pulse), corresponding to the condition of helicity preservation [34]. In this case, the output state becomes a frequency superposition of only $|\psi_+^o(\omega_1,\omega_2)\rangle$ states.

(3) If $\alpha(\omega) = 0$ (within the spectral width of the incident pulse), corresponding to the condition of total conversion of helicity [34]. In this case, $A_\chi = 0$ and thus, the output state also becomes a frequency superposition of only $|\psi_+^o(\omega_1,\omega_2)\rangle$ states.

(4) If $\alpha(\omega) = \pm\beta(\omega)$ (within the spectral width of the incident pulse), corresponding to the situation where the incident light only excites either magnetic or electric modes of the nanostructure [34–36]. In this case, $A_\psi = A_\chi$. Thus, the output state is a superposition of output $|\psi_+^o(\omega_1,\omega_2)\rangle$ and $|\chi_+^o(\omega_1,\omega_2)\rangle$ states with the same amplitude, and the differences in time delays and frequency shifts between the output pulses become zero ($\Delta\tau = 0$ and $\Delta F = 0$). This situation is discussed in more detail at the end of Sec. IV C.

(5) If both $\alpha(\omega)$ and $\beta(\omega)$ are almost constant in a spectral range given by σ. From Eqs. (19)–(22), we find that this case leads to $\Delta F \approx 0$ and $\Delta\tau \approx 0$.

From the above conditions, we can expect a substantial loss of purity if an incident nonmonochromatic pulse ($\sigma \neq 0$) excites both electric and magnetic resonances of the nanostructure [thus, $\alpha(\omega_{\text{in}}) \neq \pm\beta(\omega_{\text{in}}) \neq 0$], while $\alpha(\omega)$ and $\beta(\omega)$ change abruptly near the illumination frequency.

E. Other excitation states

So far, we considered the loss of purity when the incident state is $|\Psi_+^i\rangle$ [Eq. (3)]. Next, we consider the other input states that are frequency suppositions of the rest of the elements of the basis. First, we consider the state

$$|\Psi_-^i\rangle = \iint d\omega_1 d\omega_2 \phi(\omega_1,\omega_2)|\psi_-^i(\omega_1,\omega_2)\rangle, \tag{30}$$

with $|\psi_-^i(\omega_1,\omega_2)\rangle = \frac{1}{2}[\hat{a}_i^\dagger(\omega_1)\hat{a}_i^\dagger(\omega_2) - \hat{b}_i^\dagger(\omega_1)\hat{b}_i^\dagger(\omega_2)]|0\rangle$ [Eq. (1a)]. Notice that this state differs from the state $|\Psi_+^i\rangle$ just in the phase of the superposition of the two-photon modes. To obtain the output state, we proceed in the same manner as in Sec. III B by using the transformation given in Eq. (11), which gives

$$\begin{aligned}|\Psi_-^o\rangle = \iint \phi(\omega_1,\omega_2)\{&[\alpha(\omega_1)\alpha(\omega_2) - \beta(\omega_1)\beta(\omega_2)] \\ &\times |\psi_-^o(\omega_1,\omega_2)\rangle + [\alpha(\omega_1)\beta(\omega_2) + \beta(\omega_1)\alpha(\omega_2)] \\ &\times |\chi_-^o(\omega_1,\omega_2)\rangle\} d\omega_1 d\omega_2.\end{aligned} \tag{31}$$

Due to the use of indistinguishable photons ($\phi(\omega_1,\omega_2) = \phi(\omega_2,\omega_1)$), $\iint d\omega_1 d\omega_2 \phi(\omega_1,\omega_2)[\alpha(\omega_1)\beta(\omega_2) + \beta(\omega_1)\alpha(\omega_2)]|\chi_-^o(\omega_1,\omega_2)\rangle = 0$ [similar to Eq. (34), below], and the only contribution to $|\Psi_-^o\rangle$ are the $|\psi_-^o(\omega_1,\omega_2)\rangle$ states,

$$\begin{aligned}|\Psi_-^o\rangle = \iint \phi(\omega_1,\omega_2)&[\alpha(\omega_1)\alpha(\omega_2) \\ &- \beta(\omega_1)\beta(\omega_2)]|\psi_-^o(\omega_1,\omega_2)\rangle d\omega_1 d\omega_2.\end{aligned} \tag{32}$$

Thus, the detected density matrix of this output state [Eq. (5)] has only one element and it is pure. This result could also have been expected from the mirror and cylindrical symmetries of this particular state and of the nanostructure, as discussed in Refs. [19,20]. These results show that the input states $|\Psi_+^i\rangle$ and $|\Psi_-^i\rangle$ behave very differently when interacting with the considered nanostructures. Even when we are considering nonmonochromatic input states, one of them ($|\Psi_-^i\rangle$) will always remain pure, while the other one ($|\Psi_+^i\rangle$) can lose its purity.

Next, we consider the two other states, starting with

$$|X_-^i\rangle = \iint d\omega_1 d\omega_2 \phi(\omega_1,\omega_2)|\chi_-^i(\omega_1,\omega_2)\rangle, \tag{33}$$

with $|\chi_-^i(\omega_1,\omega_2)\rangle = \frac{1}{2}[\hat{a}_i^\dagger(\omega_1)\hat{b}_i^\dagger(\omega_2) - \hat{b}_i^\dagger(\omega_1)\hat{a}_i^\dagger(\omega_2)]|0\rangle$ [Eq. (1b)].

The state $|\chi_-^i(\omega_1,\omega_2)\rangle$ is antisymmetric under permutation of the frequencies. Thus, the incident state $|X_-^i\rangle$ becomes zero (for the two-photon spectral function that we use),

$$\begin{aligned}|X_-^i\rangle = \iint \phi(\omega_1,\omega_2)&\frac{1}{2}[\hat{a}_i^\dagger(\omega_1)\hat{b}_i^\dagger(\omega_2) - \\ &-\hat{b}_i^\dagger(\omega_1)\hat{a}_i^\dagger(\omega_2)]|0\rangle d\omega_1 d\omega_2 = 0,\end{aligned} \tag{34}$$

which means that this state cannot be generated, and, hence, there is no output state for this case.

Finally, we consider the incident state

$$|X_+^i\rangle = \iint d\omega_1 d\omega_2 \phi(\omega_1,\omega_2)|\chi_+^i(\omega_1,\omega_2)\rangle, \tag{35}$$

with $|\chi_+^i(\omega_1,\omega_2)\rangle = \frac{1}{2}[\hat{a}_i^\dagger(\omega_1)\hat{b}_i^\dagger(\omega_2) + \hat{b}_i^\dagger(\omega_1)\hat{a}_i^\dagger(\omega_2)]|0\rangle$ [Eq. (1b)]. Again, we proceed as in Sec. III B and obtain the output state,

$$\begin{aligned}|X_+^o\rangle = \iint \phi(\omega_1,\omega_2)\{&[\alpha(\omega_1)\alpha(\omega_2) + \beta(\omega_1)\beta(\omega_2)] \\ &\times |\chi_+^o(\omega_1,\omega_2)\rangle + [\alpha(\omega_1)\beta(\omega_2) + \beta(\omega_1)\alpha(\omega_2)]\end{aligned}$$

$$\times\ |\psi_+^o(\omega_1,\omega_2)\rangle\}d\omega_1 d\omega_2$$
$$= [C_\psi(\omega_1,\omega_2)|\chi_+^o(\omega_1,\omega_2)\rangle + C_\chi(\omega_1,\omega_2)$$
$$\times\ |\psi_+^o(\omega_1,\omega_2)\rangle], \tag{36}$$

which is the same result obtained for the output state $|\Psi_+^o\rangle$ [Eq. (13)] except that the coefficients $C_\psi(\omega_1,\omega_2)$ and $C_\chi(\omega_1,\omega_2)$ of the states $|\chi_+^o(\omega_1,\omega_2)\rangle$ and $|\psi_+^o(\omega_1,\omega_2)\rangle$ are interchanged. By using Eq. (5), we arrive to a similar output postselected density matrix to that of the $|\Psi_+^o\rangle$ state, but with interchanged elements, i.e., the $\hat{\varrho}^o_{\psi_+,\psi_+}$, $\hat{\varrho}^o_{\chi_+,\chi_+}$, $\hat{\varrho}^o_{\psi_+,\chi_+}$, and $\hat{\varrho}^o_{\chi_+,\psi_+}$ density matrix elements of the output state $|\Psi_+^o\rangle$ are equal to the $\hat{\varrho}^o_{\chi_+,\chi_+}$, $\hat{\varrho}^o_{\psi_+,\psi_+}$, $\hat{\varrho}^o_{\chi_+,\psi_+}$, and $\hat{\varrho}^o_{\psi_+,\chi_+}$ elements of the output state $|X_+^o\rangle$, respectively. These changes do not affect the loss of purity, and thus, the output postselected density matrix obtained for $|X_+^o\rangle$ has the same purity as the density matrix obtained for $|\Psi_+^o\rangle$.

IV. LOSS OF PURITY DUE TO THE SCATTERING BY A SILICON SPHERICAL NANOPARTICLE

In this section, we apply the model framework described above and study the loss of purity of the quantum state $|\Psi_+^i\rangle$ [Eq. (3)] when scattered by a silicon spherical nanoparticle of radius $R = 250$ nm placed in vacuum (the permittivity of silicon is obtained from Ref. [37]). In this way, we show, using an experimentally relevant system, how our theoretical model can be applied. We choose this particular nanoparticle as a study case since dielectric nanoparticles show substantially smaller intrinsic losses than their plasmonic (metallic) counterparts, making them especially suitable for the manipulation of quantum states of light.

To analyze the loss of purity in this scenario, we first obtain, in Sec. IV A, the helicity-splitting coefficients that define the quantum transformation [Eq. (11)] of states of light with a specific angular momentum and polarization scattered by the silicon spherical nanoparticle. In Sec. IV C, we use these coefficients to calculate the output state of the interaction of an incident $|\Psi_+^i\rangle$ state with the nanoparticle, and we find that the output scattered state can lose its quantum purity. We then proceed to analyze the loss of purity at the end of the same subsection.

A. Classical response: helicity-splitting coefficients

As we discussed in Sec. III, the helicity-splitting coefficients determining the transformation of quantum states can be obtained from classical calculations of the fields scattered by the nanoparticle. In particular, here we obtain the fields scattered by the nanoparticle using Mie theory as discussed in Appendix. We consider incident illumination close to that in experimental configurations: A right circularly polarized Laguerre-Gauss LG_0^1 mode [see Eq. (A2) of Appendix] with spatial width $w_0 = 0.5$ mm focused at the center of the nanoparticle by a high-numerical aperture lens (NA = 0.9) with focal length $f = 1$ mm (see scheme in Fig. 5). The incident Laguerre-Gauss beam has a well-defined orbital angular momentum and spin, with $l = +1$ and $s = -1$, respectively. Thus, this incident beam corresponds to $\boldsymbol{E}^i_{-1}$ in the notation introduced right before Eq. (10), i.e., the electric field for an incident beam with $m = 0$ and $\Lambda = -1$. Figure 6 (left panel) shows the spatial distribution of the phase and intensity of the input beam at the aperture of the lens for an incident monochromatic illumination of (vacuum) wavelength $\lambda = 1011$ nm.

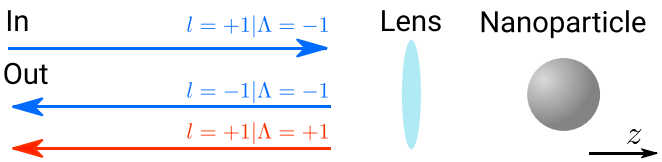


FIG. 5. Scheme of the classical scattering by a silicon spherical nanoparticle. A Laguerre-Gauss beam with $m = 0$, $\Lambda = -1$ ($l = +1$), and width $w_0 = 0.5$ mm propagates along the positive z axis toward a $R = 250$ nm silicon [37] spherical nanoparticle situated in vacuum. The incident beam is focused on the center of the nanoparticle with a high-numerical-aperture lens (NA = 0.9) and focal length $f = 1$ mm. The light backscattered by the nanoparticle is collected and collimated with the same lens and separated into the two different helicities $\Lambda = +1$ and $\Lambda = -1$. Each helicity contribution is then coupled to a single-mode fiber before reaching the detector.

The lens used to focus the incident beam also collects the backscattered light, corresponding to $\boldsymbol{E}^{s(-1)}$ in Eq. (10), i.e., the fields scattered by the nanoparticle under $\boldsymbol{E}^i_{-1}$ illumination. Figure 6 (right panel) shows the spatial field distribution of $\boldsymbol{E}^{s(-1)}$ after being collimated by the lens and being separated into its two helicity contributions, one with $\Lambda = +1$ and another with $\Lambda = -1$ (scheme in Fig. 5). Since the output collimated beams are paraxial, we can determine the spin and orbital angular momentum for each helicity contribution of

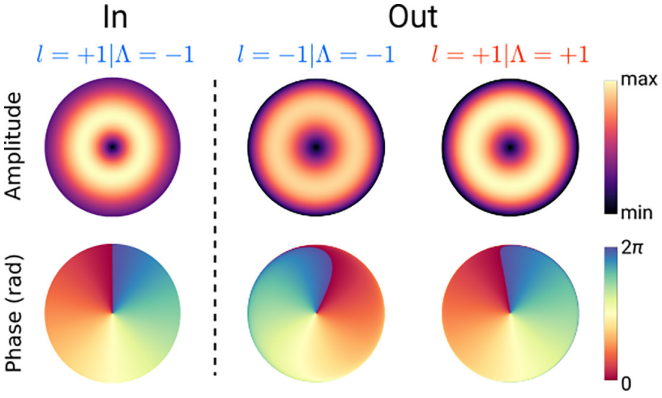


FIG. 6. Spatial distribution of the amplitude (top row) and phase (bottom row) of the input and output electric fields for a monochromatic illumination with wavelength $\lambda = 1011$ nm. The studied system consists of a silicon spherical nanoparticle of radius $R = 250$ nm illuminated by a focused $l = +1$, $m = 0$ Laguerre-Gauss beam as indicated in Fig. 5. The input and output fields are both plotted in the same plane of the aperture of the lens. The amplitude of the input electric field (first column) is normalized to its maximum value. The output beam (second and third columns) is decomposed into the two different contributions with different circular polarizations corresponding to different helicity values, as indicated in the figure (the left and right polarized contributions of the output beam correspond to $\Lambda = -1$ and $\Lambda = +1$, respectively). The amplitude of both output contributions is normalized to the maximum of the output field with helicity $\Lambda = +1$.

$\boldsymbol{E}^{s(-1)}$. Specifically, $s=-1$ and $l=+1$ for the $\Lambda=+1$ and $m=0$ contribution, and $s=+1$ and $l=-1$ for the $\Lambda=-1$ and $m=0$ contribution. Note that the spin and helicity have opposite signs for the backscattered field, as the output beam propagates along the negative z direction.

To obtain the helicity-splitting coefficients, we use Eq. (10). In this equation, the α_{-1} and β_{-1} coefficients are obtained by projecting $\boldsymbol{E}^{s(-1)}$ onto the output modes $\boldsymbol{E}^{o}_{+1}$ and $\boldsymbol{E}^{o}_{-1}$, corresponding to electromagnetic modes of the single-mode fibers introduced above. The output mode $\boldsymbol{E}^{o}_{-1}$ corresponds to $m=0$, $\Lambda=-1$, and $\boldsymbol{E}^{o}_{+1}$ to $m=0$, $\Lambda=+1$. Here, we consider the simple situation where $\boldsymbol{E}^{o}_{+1}$ ($\boldsymbol{E}^{o}_{-1}$) corresponds to a Laguerre-Gauss LG_0^1 (LG_0^{-1}), same as for the input beam, but in this case the output Laguerre-Gauss modes propagate toward the negative z direction. Because the Laguerre-Gauss output modes are paraxial, we can assign the helicity directly to the spin and, thus, to circular polarization: the $\Lambda=+1$ beam has $s=-1$ corresponding to a circular right polarization unitary vector $\boldsymbol{v}_- = (-1_x, i_y, 0_z)/\sqrt{2}$ and $\Lambda=-1$ has $s=+1$ corresponding, within the paraxial approximation, to a circular left polarization unitary vector $\boldsymbol{v}_+ = (1_x, i_y, 0_z)/\sqrt{2}$. Finally, using Eq. (10), we can directly obtain the helicity-splitting coefficients:

$$\alpha_{-1}(\omega) = \iint_{\mathcal{A}} d\mathcal{A}\left[\mathrm{LG}_0^{-1}(\boldsymbol{r})\boldsymbol{v}_- e^{-i\omega t}\right]^* \cdot \boldsymbol{E}^{s(-1)},$$
$$\beta_{-1}(\omega) = \iint_{\mathcal{A}} d\mathcal{A}\left[\mathrm{LG}_0^{+1}(\boldsymbol{r})\boldsymbol{v}_+ e^{-i\omega t}\right]^* \cdot \boldsymbol{E}^{s(-1)}. \quad (37)$$

The integrating area $\mathcal{A}$ in Eq. (37) corresponds to the surface of the aperture of the lens (same area of the fields shown in Fig. 6).

In a similar manner, we can calculate α_{+1} and β_{+1}, for the fields scattered by the nanoparticle when illuminated with $m=0$, $\Lambda=+1$, and Laguerre-Gauss mode LG_0^{-1}. However, the detection scheme that we have proposed ensures that the input and the output fields are related by a mirror transformation. This imposes that $\alpha_{+1}=\alpha_{-1}=\alpha$ and $\beta_{+1}=\beta_{-1}=\beta$, and thus, we can use the simple transformation introduced in Eq. (11). This can also be verified using the equivalent of Eq. (37) for α_{+1} and β_{+1}.

We show in Figs. 7(a) and 7(b) the amplitude and phase spectra of α (blue line) and β (orange line), obtained by evaluating Eq. (37) for different wavelengths $\lambda \in [975, 1150]$ nm. Figure 7(a) shows that the spectra of the amplitudes $|\alpha(\omega)|$ (blue line) and $|\beta(\omega)|$ (orange line) exhibit two clear peaks: A relatively broad maxima centered at $\lambda \approx 1040$ nm and a sharp peak centered at $\lambda \approx 1000$ nm. In the proximity of these two peaks, the phase of the coefficients [$\arg\{\alpha(\omega)\}$ and $\arg\{\beta(\omega)\}$] varies rapidly, particularly near the sharp peak [Fig. 7(b)].

B. Analysis of the contributions of the different resonances of the nanoparticle to the helicity-splitting coefficients

We next analyze the nature of the peaks of $|\alpha(\omega)|$ and $|\beta(\omega)|$ in Fig. 7(a) by using Mie theory, which fully includes the effect of all decay channels. To that end, we show in Fig. 8 (black line) the classical scattering cross-section spectrum σ_{sca} of the $R=250$ nm silicon spherical nanoparticle under the illumination of the focused $l=+1$, $m=0$

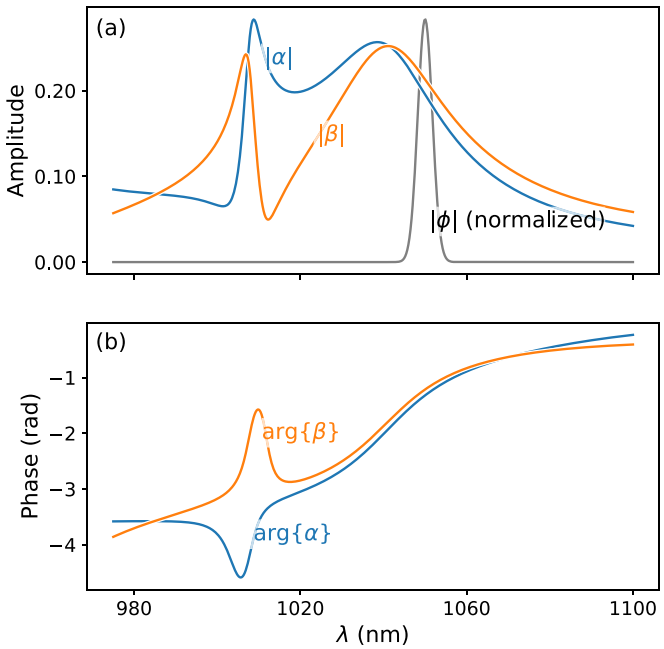


FIG. 7. (a) Amplitude and (b) phase of the helicity-splitting coefficients α (blue line) and β (orange line) that are obtained from the classical scattering calculation, as a function of wavelength λ. The coefficients are obtained for a silicon spherical nanoparticle of radius $R=250$ nm illuminated by a focused $l=+1$, $m=0$ monochromatic Laguerre-Gauss beam as indicated in Fig. 5. For reference, we also present in panel (a) the spectral amplitude $|\phi|$ (normalized to the maximum amplitude of $|\alpha|$) of an incident pulse centered at $\lambda_{\mathrm{in}}=1060$ nm. This allows us to compare the spectral width of the two-photon pulse with the width of the spectral features of the silicon nanoparticle response.

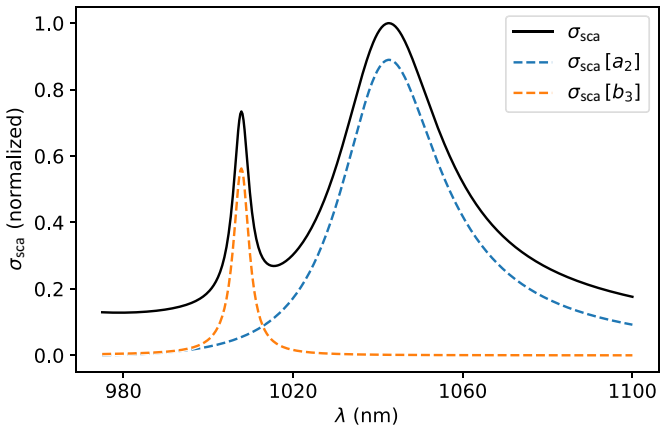


FIG. 8. Different contributions to the scattering cross section of the silicon [37] spherical nanoparticle of radius $R=250$ nm studied in section IV. The nanoparticle is illuminated by a monochromatic Laguerre-Gauss beam with $l=1$, $s=-1$, and width $w_0=0.5$ mm that is focused at the center of the spherical nanoparticle by a lens of NA $=0.9$ and $f=1$ mm. The solid black line corresponds to the total scattering cross section of the system σ_{sca} and the dashed lines to the two main contributions to σ_{sca}, due to the electric quadrupolar ($\sigma_{\mathrm{sca}}[a_2]$ proportional to $|a_2(\omega)|^2$ in Eq. (38), dashed blue line) and the magnetic octupolar ($\sigma_{\mathrm{sca}}[b_3](\omega)$ proportional to $|b_3(\omega)|^2$ in Eq. (38), dashed orange line) modes of the nanoparticle.

Laguerre-Gauss beam. $\sigma_{\rm sca}$ presents again two clear peaks, a broad one centered at $\lambda \approx 1040$ nm and a narrow peak centered at $\lambda \approx 1010$ nm. The spectral position of the maximum of these two peaks is very close to the maximum of the two peaks of the $|\alpha(\omega)|$ and $|\beta(\omega)|$ helicity-splitting coefficients [shown in Fig. 7(a)], which indicates that the peaks of the helicity-splitting coefficients are related to the excitation of the resonances of the nanoparticles. To analyze which resonances are excited at these spectral positions, we decompose $\sigma_{\rm sca}$ as a sum of the contributions of each multipole [38]:

$$\sigma_{\rm sca} = \frac{2\pi}{k^2}\sum_{n=0}^{\infty}|C_n(\omega)|^2(|a_n(\omega)|^2 + |b_n(\omega)|^2), \tag{38}$$

where C_n is given by Eq. (A4) of Appendix and a_n and b_n [in Eqs. (A8) and (A9) of Appendix] are the scattering coefficients of the electric and magnetic multipoles, respectively.

In Fig. 8, we plot the two contributions given by the scattering coefficients a_2 (dashed blue line) and b_3 (dashed orange line) in Eq. (38). We find that the broad peak of the total scattered cross section centered at $\lambda \approx 1040$ nm is due to the term proportional to $|a_2|^2$ in Eq. (38), which indicates that this peak results from the excitation of an electric quadrupolar resonance in the nanoparticle [39]. The term proportional to $|b_3|^2$ causes the narrow peak centered at $\lambda \approx 1010$ nm and corresponds to the excitation of an octupolar magnetic resonance [39].

C. Quantum response: Analysis of the purity of the scattered state

With the results of $\alpha(\omega)$ and $\beta(\omega)$ shown in Figs. 7(a) and 7(b) we can now calculate the postselected output density matrix $\hat{\varrho}^o$ [using Eqs. (5)–(14)] when the silicon spherical nanoparticle is illuminated by the focused entangled input state $|\Psi_+^i\rangle$. The input state in this case is a two-photon Gaussian pulse with a bandwidth of $\sigma = 3$ THz. Figures 9(a) and 9(b) show the output postselected density matrix, with an illumination field spectrum centered at $\lambda_{\rm in} = 1003$ nm (exciting one nanoparticle resonance) and $\lambda_{\rm in} = 1025$ nm (in between nanoparticle resonances), respectively. This figure shows that the output scattered states are different depending on the wavelength of the illumination due to changes in the helicity-splitting coefficients in this range of wavelengths. Furthermore, the output state is pure ($\mathcal{L}_o \approx 0$) when illuminated at $\lambda_{\rm in} = 1025$ nm, but there is a loss of quantum purity ($\mathcal{L}_o \approx 0.05 > 0$) when illuminated at $\lambda_{\rm in} = 1003$ nm, as indicated in the figure. We emphasize that $\mathcal{L}_0 \approx 0$ is possible despite not collecting all photons with the lens because we are considering the two-photon postselected state.

To further study the loss of quantum purity, we show in Fig. 10(a) (solid black line) $\mathcal{L}_o$ of the output state as a function of the central wavelength of the pulse $\lambda_{\rm in} = 2\pi c_0/\omega_{\rm in}$. We find two clear peaks situated at $\lambda_{\rm in} \approx 1003$ nm and $\lambda_{\rm in} = 1012$ nm, where the purity loss becomes significant ($\mathcal{L}_o \sim 0.1$).

To understand the cause of the loss of purity, we examine the quasimonochromatic approximation discussed in Sec. III B. According to this approximation, the output state is a combination of two time-delayed and frequency-shifted states [40]. We show in Fig. 10(b), the spectral dependence of the time delays τ_Ψ (solid blue line) and τ_χ (solid red line), and in Fig. 10(c) we show the corresponding values of the frequency shifts $\sigma^2 F_\Psi$ and $\sigma^2 F_\chi$. The loss of purity can be calculated in the quasimonochromatic approximation by using Eq. (29). Figure 10(a) (green dashed line) shows the result of this calculation. There is a very good agreement between the results obtained with the approximated expression (green dashed line) and the exact expression of the loss of purity (solid black line). Further, the quasimonochromatic model provides a clear explanation for the results, as the loss of purity is highest when there is a greater difference in time delays and frequency shifts, as observed in the region of 1000 nm $\lesssim \lambda_{\rm in} \lesssim$ 1020 nm of Figs. 10(a)–10(c).

Examining the equations of the frequency shift and time delays in the output pulse [Eqs. (19)–(22)], it is possible to note that the differences in frequency shifts and time delays maximize in the spectral region where the spectral behaviors of $\alpha(\omega)$ and $\beta(\omega)$ are strongly marked within the spectral width of the incident pulse. Indeed, by inspecting the helicity-splitting coefficients in Figs. 7(a) and 7(b), we can observe that the spectral region where the differences between the helicity-splitting coefficients are largest corresponds to 1000 nm $\lesssim \lambda_{\rm in} \lesssim$ 1020 nm, where the loss of purity is maximized.

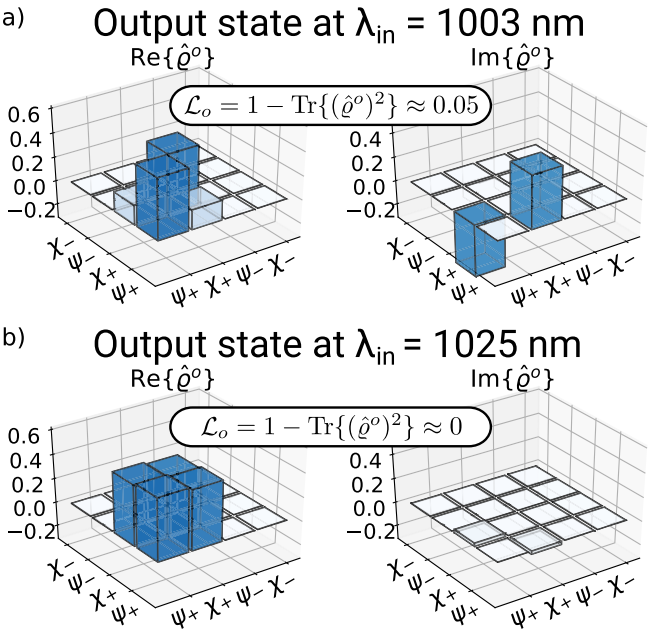


FIG. 9. Real (left) and imaginary (right) components of $\hat{\varrho}^o$, the postselected density matrix of the output state $|\Psi_+^o\rangle$ that results from the scattering of the incident input state $|\Psi_+^i\rangle$ in Fig. 1 by a silicon spherical nanoparticle of radius $R = 250$ nm (more details of the system in the caption of Fig. 5). Panels (a) and (b) correspond to $\hat{\varrho}^o$ calculated for an incident pulsed state of width $\sigma = 3$ THz at central wavelength $\lambda_{\rm in} = 1003$ nm and $\lambda_{\rm in} = 1025$ nm respectively. We indicate the loss of purity $\mathcal{L}_o$ for each illumination, where $\mathcal{L}_o \approx 0.05 > 0$ in panel (a) indicates that the output state for $\lambda_{\rm in} = 1003$ nm is not pure, and $\mathcal{L}_o \approx 0$ in panel (b) indicates that the output state for $\lambda_{\rm in} = 1025$ nm is pure.

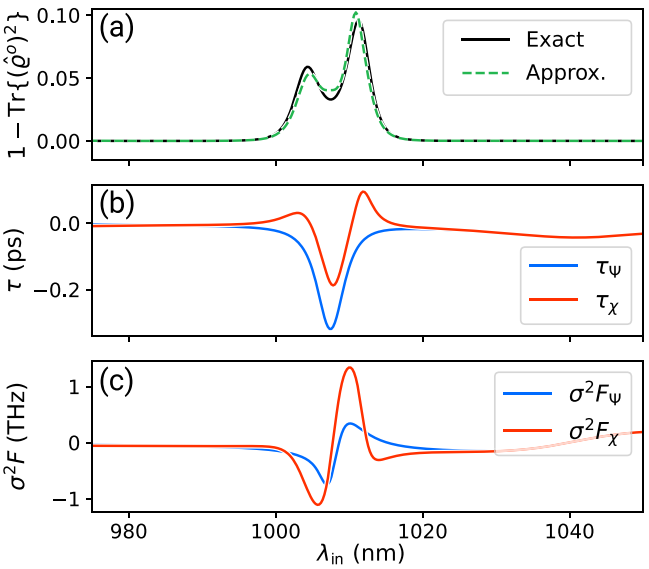


FIG. 10. Analysis of the purity loss for a focused incident $|\Psi_+^i\rangle$ state interacting with a $R = 250$ nm silicon [37] spherical nanoparticle in vacuum. (a) Spectrum of the purity loss $1 - \mathrm{Tr}\{(\hat{\varrho}^o)^2\}$. The solid black line corresponds to the purity loss of the numerically calculated density matrix [Eq. (5)] of the output state [Eq. (13)] and the dashed green line to the result of the approximated Eq. (29). (b) Spectrum of the time delay of the two two-photon modes of the total output state according to Eqs. (20) and (22). The solid blue line corresponds to τ_Ψ and the solid red line to τ_χ. (c) Spectrum of the frequency shift of the two two-photon modes of the total output state according to Eqs. (19) and (21). The solid blue line corresponds to $\sigma^2 F_\Psi$ and the solid red line to $\sigma^2 F_\chi$.

D. Influence of the magnetic and electric resonances on the loss of purity

In Sec. III B, we discuss that an abrupt spectral variation of $\alpha(\omega)$ and of $\beta(\omega)$ can cause the loss of purity of the output state. Interestingly, we tracked down such fast spectral variation to the simultaneous excitation of both magnetic octupole and electric quadrupole resonances of the nanoparticle. In fact, we show next that the loss of purity only occurs when the nanoparticle supports both electric and magnetic resonances.

A nanoparticle that only supports magnetic resonances satisfies $a_n = 0$ for all n in Eqs. (A6) and (A7) of Appendix. In this case, a detailed analysis of the fields scattered by the nanoparticle when illuminated by beams with well-defined angular momentum leads to $\alpha(\omega) = -\beta(\omega)$ [34,38,39]. On the other hand, if a nanoparticle only supports electric resonances, then $b_n = 0$ for all n in Eqs. (A6) and (A7), and in this case we obtain $\alpha(\omega) = \beta(\omega)$. From the intuitive quasimonochromatic picture introduced in Sec. III B, $\alpha(\omega) = \pm\beta(\omega)$ constitutes two special cases, both leading to $\tau_\psi = \tau_\chi$ and $F_\psi = F_\chi$ in Eqs. (19)–(22), i.e., there is no difference in time delays nor frequency shift between the output pulses, and thus, the loss of purity in Eq. (29) becomes zero.

Further, it is not necessary to adopt the quasimonochromatic approximation to show that the output state is always pure for $\alpha(\omega) = \pm\beta(\omega)$. Using Eqs. (13)–(14b), we obtain the output state in these cases,

$$|\Psi_+^o[\alpha = \pm\beta]\rangle = \iint \phi(\omega_1, \omega_2)[2\alpha(\omega_1)\alpha(\omega_2)] \times [|\psi_+^o(\omega_1, \omega_2)\rangle \pm |\chi_+^o(\omega_1, \omega_2)\rangle]d\omega_1 d\omega_2. \tag{39}$$

In this expression, $|\psi_+^o(\omega_1, \omega_2)\rangle$ and $|\chi_+^o(\omega_1, \omega_2)\rangle$ are multiplied by the same spectral function $\phi(\omega_1, \omega_2)[2\alpha(\omega_1)\alpha(\omega_2)]$. This shared weighting function causes the detected output state to be pure, as directly proved by inserting Eq. (39) in Eq. (5). We obtain an output detected density matrix with only four nonzero terms, $\hat{\varrho}^o_{\psi_+,\psi_+} = \hat{\varrho}^o_{\chi_+,\chi_+} = 1/2$, $\hat{\varrho}^o_{\psi_+,\chi_+} = \hat{\varrho}^o_{\chi_+,\psi_+} = \pm 1/2$ (from $\alpha(\omega) = \pm\beta(\omega)$), which is an idempotent matrix, (*i.e.*, $(\hat{\varrho}^o)^n = \hat{\varrho}^o$), corresponding to a pure state, $\mathrm{Tr}\{(\hat{\varrho}^o)^2\} = 1 \rightarrow \mathcal{L}_o = 0$. Thus, the loss of purity can be attributed to the simultaneous excitation of electric and magnetic resonances of the nanoparticle.

V. CONCLUSIONS

In summary, in this work we provide a framework to treat the scattering of a pulsed quantum two-photon state in modes of well-defined angular momentum and helicity interacting with a rotationally symmetric nanostructure. This framework fully takes into account the effect of absorption and scattering losses, and the collection of only a fraction of the emitted photons. We find that the interaction of entangled photons with nanostructures can produce a loss of purity of the incident state, even when the nanostructure is smaller than the wavelength of the incident field. We apply our framework to analyze the loss of purity in a realistic scenario, a silicon spherical nanoparticle illuminated by a focused two-photon state generated by, for example, an SPDC process, where the two photons are indistinguishable. Further, we developed a simple physical picture that explains the loss of quantum purity as a consequence of a difference in time delays and a frequency shift between the two-photon modes of the output state. Importantly, these frequency shifts and time delays can be traced back to the spectral width of the incident pulsed states and the excitation of different optical resonances of the nanoparticle.

Our framework and findings can be extended to treat the scattering of quantum states of light by other nanostructures using more complex scattering matrices, which can be obtained from numerical methods or analytical calculations. This can be useful in preventing the loss of purity in quantum information applications handled at the nanoscale.

ACKNOWLEDGMENTS

G.M.-T. and J.L.-A. acknowledge financial support through Grant No. PID2022-143268NB-I00 and Á.N., C.M.-E., R.E., and J.A. acknowledge financial support through Grant No. PID2022-139579NB-I00, both funded by MICIU/AEI/10.13039/501100011033 and by ERDF, EU. Á.N., R.E., C.M.-E., J.A, and G.M.-T. acknowledge financial support from the Department of Science, Universities and Innovation of the Basque Government through Project Ref. No. IT-1526-22. Á.N., R.E., J.A., and

G.M.-T. acknowledge financial support by the European Commission-NextGenerationEU (Regulation EU 2020/2094), through CSIC's Quantum Technologies Platform (QTEP) (Project No. 20219PT023). Á.N. acknowledges funding from MCIN/AEI/10.13039/501100011033 and "ESF Investing in your future" through Project Ref. No. BES-2017-080073.

DATA AVAILABILITY

The data that support the findings of this article are openly available [46].

APPENDIX: DETAILS OF THE CLASSICAL CALCULATIONS

The interaction between quantum states of light and a spherical nanoparticle is described by Eq. (11) in the main text, and it is encoded on the $\alpha(\omega)$ and $\beta(\omega)$ helicity-splitting coefficients. This section describes all the steps required to obtain these two coefficients for the system studied in the main text.

$\alpha(\omega)$ and $\beta(\omega)$ can be obtained from the analysis of the fields scattered by the nanostructure when it is illuminated by classical light characterized by the same spatial dependence of the electromagnetic fields as the quantum states considered. We can use the classical response as an input to later describe the quantum behavior because Maxwell's equations determine how the electromagnetic modes of classical and quantized states of light evolve [32].

The system that we study (see Fig. 5 of the main text) consists of a spherical nanoparticle that scatters a highly focused Laguerre-Gauss beam. Before being focused by the lens, the incident Laguerre-Gauss beam is characterized by total angular momentum $m = 0$ and spin $s = -1$ (and thus, orbital angular momentum $l = m - s = +1$). We note that the values of $\alpha(\omega)$ and $\beta(\omega)$ are independent of the chosen s for $m = 0$ incident beams due to the mirror symmetry of the nanostructure. This input beam propagates along the positive z axis and is focused by an aplanatic lens of a high-numerical aperture NA $= 0.9$ placed at the focal length $f = 1$ mm from the center of the nanoparticle. The backscattered field (i.e., the scattering of the nanoparticle in the direction of negative z) is collected and collimated by the same lens. The collimated field is separated into two helicity contributions. This separation can be achieved experimentally with a polarized 50/50 beam splitter because the backscattered beam has a planar wavefront after the collimation, so that there is a direct relationship between the helicity Λ and the polarization of the field: The backscattered beams with left or right circular polarizations have spin $s = +1$ ($\Lambda = -1$) or $s = -1$ ($\Lambda = +1$), respectively (Λ is defined as the spin projected in the direction of propagation).

To obtain the $\alpha(\omega)$ and $\beta(\omega)$ helicity-splitting coefficients, we describe the field profile of the $m = 0$, $s = -1$ Laguerre-Gauss mode to be focused by the lens following the standard form [41]:

$$\boldsymbol{E}^{\mathrm{LG}}_{\Lambda}(\rho, \varphi_{\mathrm{p}}) = A_0^{\mathrm{LG}^l_q}(\rho, \varphi_{\mathrm{p}})\hat{\boldsymbol{v}}_s, \tag{A1}$$

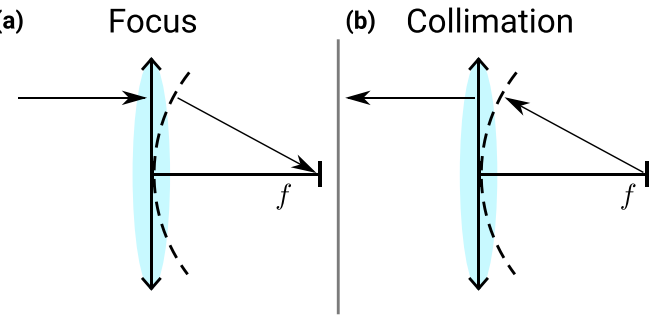


FIG. 11. Scheme of the (a) focusing and (b) collimation process described by the aplanatic lens model. In the focusing process, the field incident on the aperture of the lens (vertical arrow in the shaded blue area) is mapped into a spherical surface of radius f (dashed line) and then rotated such that it propagates toward the focus (i.e., the center of this spherical surface). The collimation corresponds to the inverse process, so that the field is evaluated in the same spherical surface, rotated, and then mapped into the aperture of the lens.

with

$$\mathrm{LG}^l_q(\rho, \varphi_{\mathrm{p}}) = \sqrt{\frac{2q!}{\pi(q+|l|)!}}\frac{1}{w_0}\left(\frac{\rho\sqrt{2}}{w_0}\right)^{|l|} \times \exp\left(\frac{-\rho^2}{w_0^2}\right)L^l_q\left(\frac{2\rho^2}{w_0^2}\right)\exp(il\varphi_{\mathrm{p}}), \tag{A2}$$

the Laguerre-Gauss mode, ρ and φ_{p} are the radial and polar angle coordinates, respectively, at the aperture of the lens (with $\rho = 0$ being the center of the lens), l is the Azimuthal order (number of times the phase twists around the origin), q the number of radial nodes of the incident Laguerre-Gauss beam (for this work $q = 0$), $w_0 = 0.5$ mm the width of the beam, L^l_q the generalized Laguerre polynomials [42], and $\boldsymbol{v}_s$ the spin unit vectors, which in Cartesian coordinates are written as $\boldsymbol{v}_+ = (1_x, i_y, 0_z)/\sqrt{2}$ and $\boldsymbol{v}_- = (-1_x, i_y, 0_z)/\sqrt{2}$. The field in Eq. (A1) is normalized such that $\int_0^\infty \rho d\rho \int_0^{2\pi} d\varphi_p \, |\boldsymbol{E}^{\mathrm{LG}}_{\Lambda}|^2 = |A_0|^2$.

The beam given by Eq. (A1) is focused by the lens. We follow Ref. [38] and write the focused field as an expansion of multipoles $\boldsymbol{A}^{(\Lambda)}_{1,n}$ of different order n, which facilitates the calculation of the scattered fields using Mie's theory. The index "1" in $\boldsymbol{A}^{(\Lambda)}_{1,n}$ indicates that this basis element is proportional to the spherical Bessel function of the first kind (see Chap. 4 of Ref. [39]). The expansion considered here uses a basis such that each multipole, $\boldsymbol{A}^{(\Lambda)}_{1,n}$, has a well-defined helicity [38,43–45]. The focused electric field is

$$\boldsymbol{E}^i_{\Lambda}(r, \varphi_{\mathrm{s}}, \theta, \omega) = \sum_{n=0}^{\infty}\sqrt{2}C_n(\omega)\boldsymbol{A}^{(\Lambda)}_{1,n}(r, \varphi_{\mathrm{s}}, \theta, \omega), \tag{A3}$$

where ω is the angular frequency of the light, and r, φ_{s}, and θ are the spherical coordinates (radial, polar, and Azimuthal, respectively) with origin at the center of the nanoparticle. The coefficients C_n are given by (see Ref. [38])

$$C_n = i^{n-1}\sqrt{2n+1} \times k\sqrt{2\pi}\int_0^{\theta_{\max}}\sin(\theta)d\theta \times \left(\boldsymbol{E}^{(\Lambda)}_{\mathrm{LG}}(f\sin(\theta), 0)\cdot\hat{\boldsymbol{u}}_s\right)\sqrt{\cos(\theta)}fe^{-ikf}, \tag{A4}$$

where $\theta_{\max}$ is the maximal half angle of the lens, and $k = 2\pi/\lambda$, λ being the wavelength of light in vacuum. These coefficients are derived in Ref. [38] using the aplanatic lens model [45], schematized in Fig. 11(a). The modeling of the focusing process used to obtain Eq. (A4) can be separated into three steps. First, we map the incident electric field in the aperture of the lens onto a reference surface with coordinates $r = f$, $\varphi_s \in [0, 2\pi]$, and $\theta \in [\pi - \theta_{\max}, \pi]$ (i.e., a spherical cap situated at the focal distance f from the nanoparticle). Second, the mapped (vectorial) electric field is rotated such that from each point of the reference surface emerges a plane wave that propagates toward the focal point. Third, we obtain the field in the focal point as the sum of all these plane waves.

We next obtain the fields scattered by the nanoparticle using the expression [38]:

$$\boldsymbol{E}_{\Lambda}^{\mathrm{SC}}(r,\varphi_s,\theta,\omega) = \sum_{n=0}^{\infty} C_n(\omega)\big(V_n(\omega)\boldsymbol{A}_{3,n}^{(\Lambda)}(r,\varphi_s,\theta,\omega) + W_n(\omega)\boldsymbol{A}_{3,n}^{(-\Lambda)}(r,\varphi_s,\theta,\omega)\big), \tag{A5}$$

where the multipoles $\boldsymbol{A}_{3,n}^{(\Lambda)}$ are, in this case, proportional to the spherical Bessel functions of the third kind, and

$$V_n(\omega) = -\frac{a_n(\omega) + b_n(\omega)}{\sqrt{2}}, \tag{A6}$$

$$W_n = \frac{a_n(\omega) - b_n(\omega)}{\sqrt{2}}. \tag{A7}$$

$a_n(\omega)$ and $b_n(\omega)$ are the standard scattering coefficients in Mie's theory used to describe the contributions of the electric and magnetic modes, respectively [39],

$$a_n = \frac{n_{\mathrm{R}}^2 j_n(\zeta_0)\psi'(\zeta_0) - j_n(\zeta_0)\psi_n'(n_{\mathrm{R}}\zeta_0)}{n_{\mathrm{R}}^2 j_n(n_{\mathrm{R}}\zeta_0)\xi_n'(\zeta_0) - h_n^{(I)}(\zeta_0)\psi_n'(n_{\mathrm{R}}\zeta_0)}, \tag{A8}$$

$$b_n = \frac{j_n(n_{\mathrm{R}}\zeta_0)\psi_n'(\zeta_0) - j_n(\zeta_0)\psi_n'(n_{\mathrm{R}}\zeta_0)}{j_n(n_{\mathrm{R}}\zeta_0)\xi_n'(\zeta_0) - h_n^{(I)}(\zeta_0)\psi_n'(n_{\mathrm{R}}\zeta_0)}, \tag{A9}$$

where $n_{\mathrm{R}} = n_{\mathrm{sph}}/n_0$ is the refractive index of the sphere n_{sph} normalized by the refractive index of the medium n_0 and $\zeta_0 = 2\pi R/\lambda$. j_n is the spherical Bessel function of the first kind, and $\psi_n(\zeta_0)$ and $\xi_n(\zeta_0)$ are the Riccatti-Bessel functions of the first and third order, respectively. $\psi_n'(\cdots)$ and $\xi_n'(\cdots)$ are the derivatives of the Riccatti-Bessel functions.

The backscattered field given in Eq. (A5) is collimated through the same lens that focuses the incident beam. To model the effect of this collimation using the aplanatic lens model, we follow the inverse process of the focusing described above [Fig. 11(b)]. The backscattered field is evaluated at the spherical reference surface [dashed line in Fig. 11(b)]. We then perform the inverse rotation for the focusing process so that the propagation vectors of the scattered field become paraxial. Finally, we map the rotated field of the reference aperture into the surface of the lens. This collimation process is mathematically equivalent to the following transformation:

$$\boldsymbol{E}^{\mathrm{s}(\Lambda)}(\rho,\varphi_{\mathrm{p}},\omega) = \hat{R}(f,\varphi_{\mathrm{p}},\theta)\cdot\boldsymbol{E}_{\Lambda}^{\mathrm{SC}}(f,\varphi_s,\theta,\omega)\cos(\theta)^{-1}, \tag{A10}$$

where $\boldsymbol{E}^{\mathrm{s}(\Lambda)}$ is the collimated field, ρ and φ_{p} are the polar coordinates in the aperture of the lens (defined above), and $\hat{R}(f,\varphi_{\mathrm{p}},\theta)$ is the position-dependent Euler rotation matrix:

$$\hat{R}(f,\varphi_s,\theta) = \begin{pmatrix} \sin(\varphi_s) & -\cos(\varphi_s) & 0 \\ \cos(\varphi_s) & \sin(\varphi_s) & 0 \\ 0 & 0 & 1 \end{pmatrix}\cdot\begin{pmatrix} 1 & 0 & 0 \\ 0 & \cos(\theta) & -\sin(\theta) \\ 0 & \sin(\theta) & \cos(\theta) \end{pmatrix}\cdot\begin{pmatrix} \sin(\varphi_s) & \cos(\varphi_s) & 0 \\ -\cos(\varphi_s) & \sin(\varphi_s) & 0 \\ 0 & 0 & 1 \end{pmatrix}. \tag{A11}$$

The $\cos(\theta)^{-1}$ factor in Eq. (A10) accounts for the differences between the differential area at the reference spherical surface, dA_S, and the differential area at the aperture of the lens, dA_L [$dA_S = dA_L/\cos(\theta)$; see Chap. 3 of Ref. [45]].

Finally, we obtain the helicity-splitting coefficients $\alpha(\omega)$ and $\beta(\omega)$ by projecting $\boldsymbol{E}^{\mathrm{s}(\Lambda)}$ into the modes of a single-mode fiber connected to the detectors. The modes of these fibers have the same spatial distribution as those of the input fields. The final expression is given by Eq. (37).

[1] W. H. Zurek, Decoherence, einselection, and the quantum origins of the classical, Rev. Mod. Phys. **75**, 715 (2003).

[2] Y.-S. Kim, J.-C. Lee, O. Kwon, and Y.-H. Kim, Protecting entanglement from decoherence using weak measurement and quantum measurement reversal, Nat. Phys. **8**, 117 (2012).

[3] M. Krenn, R. Fickler, M. Fink, J. Handsteiner, M. Malik, T. Scheidl, R. Ursin, and A. Zeilinger, Communication with spatially modulated light through turbulent air across Vienna, New J. Phys. **16**, 113028 (2014).

[4] M. Krenn, M. Malik, T. Scheidl, R. Ursin, and A. Zeilinger, Quantum communication with photons, Opt. Time **18**, 455 (2016).

[5] M. Aspelmeyer, H. R. Bohm, T. Gyatso, T. Jennewein, R. Kaltenbaek, M. Lindenthal, G. Molina-Terriza, A. Poppe, K. Resch, M. Taraba, *et al.*, Long-distance free-space distribution of quantum entanglement, Science **301**, 621 (2003).

[6] T. D. Ladd, F. Jelezko, R. Laflamme, Y. Nakamura, C. Monroe, and J. L. O'Brien, Quantum computers, Nature (London) **464**, 45 (2010).

[7] M. A. Nielsen and I. Chuang, *Quantum Computation and Quantum Information* (Cambridge University Press, New York, 2002).

[8] M.-A. Lemonde, N. Didier, and A. A. Clerk, Enhanced nonlinear interactions in quantum optomechanics via mechanical amplification, Nat. Commun. **7**, 11338 (2016).

[9] L. Novotny and N. Van Hulst, Antennas for light, Nat. Photon. **5**, 83 (2011).

[10] F. Benz, M. K. Schmidt, A. Dreismann, R. Chikkaraddy, Y. Zhang, A. Demetriadou, C. Carnegie, H. Ohadi, B. De Nijs, R. Esteban, *et al.*, Single-molecule optomechanics in "picocavities", Science **354**, 726 (2016).

[11] A. Krasnok, M. Caldarola, N. Bonod, and A. Alú, Spectroscopy and biosensing with optically resonant dielectric nanostructures, Adv. Opt. Mater. **6**, 1701094 (2018).

[12] J. Lasa-Alonso, D. R. Abujetas, Á. Nodar, J. A. Dionne, J. J. Sáenz, G. Molina-Terriza, J. Aizpurua, and A. García-Etxarri, Surface-enhanced circular dichroism spectroscopy on periodic dual nanostructures, ACS Photonics **7**, 2978 (2020).

[13] O. J. Farías, V. D'Ambrosio, C. Taballione, F. Bisesto, S. Slussarenko, L. Aolita, L. Marrucci, S. P. Walborn, and F. Sciarrino, Resilience of hybrid optical angular momentum qubits to turbulence, Sci. Rep. **5**, 8424 (2015).

[14] A. H. Ibrahim, F. S. Roux, M. McLaren, T. Konrad, and A. Forbes, Orbital-angular-momentum entanglement in turbulence, Phys. Rev. A **88**, 012312 (2013).

[15] S. S. R. Oemrawsingh, X. Ma, D. Voigt, A. Aiello, E. R. Eliel, G. W. 't Hooft, and J. P. Woerdman, Experimental demonstration of fractional orbital angular momentum entanglement of two photons, Phys. Rev. Lett. **95**, 240501 (2005).

[16] S. Franke-Arnold, L. Allen, and M. Padgett, Advances in optical angular momentum, Laser Photonics Rev. **2**, 299 (2008).

[17] G. Molina-Terriza, A. Vaziri, J. Řeháček, Z. Hradil, and A. Zeilinger, Triggered qutrits for quantum communication protocols, Phys. Rev. Lett. **92**, 167903 (2004).

[18] G. Molina-Terriza, J. P. Torres, and L. Torner, Twisted photons, Nat. Phys. **3**, 305 (2007).

[19] J. Lasa-Alonso, M. Molezuelas-Ferreras, J. M. Varga, A. García-Etxarri, G. Giedke, and G. Molina-Terriza, Symmetry-protection of multiphoton states of light, New J. Phys. **22**, 123010 (2020).

[20] A. Büse, M. L. Juan, N. Tischler, V. D'Ambrosio, F. Sciarrino, L. Marrucci, and G. Molina-Terriza, Symmetry protection of photonic entanglement in the interaction with a single nanoaperture, Phys. Rev. Lett. **121**, 173901 (2018).

[21] N. Tischler, C. Rockstuhl, and K. Słowik, Quantum optical realization of arbitrary linear transformations allowing for loss and gain, Phys. Rev. X **8**, 021017 (2018).

[22] S. M. Barnett, J. Jeffers, A. Gatti, and R. Loudon, Quantum optics of lossy beam splitters, Phys. Rev. A **57**, 2134 (1998).

[23] B. Vest, M.-C. Dheur, É. Devaux, A. Baron, E. Rousseau, J.-P. Hugonin, J.-J. Greffet, G. Messin, and F. Marquier, Anti-coalescence of bosons on a lossy beam splitter, Science **356**, 1373 (2017).

[24] S. Fan, Ş. E. Kocabaş, and J.-T. Shen, Input-output formalism for few-photon transport in one-dimensional nanophotonic waveguides coupled to a qubit, Phys. Rev. A **82**, 063821 (2010).

[25] C. Cohen-Tannoudji, B. Diu, and F. Laloë, *Quantum Mechanics: Basic Concepts, Tools, and Applications* (Wiley, Weinheim, Germany, 2019), Vol. 1.

[26] A. Akimov, A. Mukherjee, C. Yu, D. Chang, A. Zibrov, P. Hemmer, H. Park, and M. Lukin, Generation of single optical plasmons in metallic nanowires coupled to quantum dots, Nature (London) **450**, 402 (2007).

[27] J. M. Varga, J. Lasa-Alonso, M. Molezuelas-Ferreras, N. Tischler, and G. Molina-Terriza, Bandwidth control of the biphoton wavefunction exploiting spatio-temporal correlations, Opt. Commun. **504**, 127461 (2022).

[28] N. Tischler, A. Buese, L. G. Helt, M. L. Juan, N. Piro, J. Ghosh, M. J. Steel, and G. Molina-Terriza, Measurement and shaping of biphoton spectral wave functions, Phys. Rev. Lett. **115**, 193602 (2015).

[29] J. B. Altepeter, E. R. Jeffrey, and P. G. Kwiat, Photonic state tomography, Adv. At. Mol. Opt. Phys. **52**, 105 (2005).

[30] R. Matloob, R. Loudon, S. M. Barnett, and J. Jeffers, Electromagnetic field quantization in absorbing dielectrics, Phys. Rev. A **52**, 4823 (1995).

[31] R. Matloob and R. Loudon, Electromagnetic field quantization in absorbing dielectrics. II, Phys. Rev. A **53**, 4567 (1996).

[32] I. Białynicki-Birula, On the wave function of the photon, Acta Phys. Pol. A **86**, 97 (1994).

[33] J. C. Schotland, A. Cazé, and T. B. Norris, Scattering of entangled two-photon states, Opt. Lett. **41**, 444 (2016).

[34] J. Olmos-Trigo, C. Sanz-Fernández, D. R. Abujetas, J. Lasa-Alonso, N. de Sousa, A. García-Etxarri, J. A. Sánchez-Gil, G. Molina-Terriza, and J. J. Sáenz, Kerker conditions upon lossless, absorption, and optical gain regimes, Phys. Rev. Lett. **125**, 073205 (2020).

[35] X. Zambrana-Puyalto, I. Fernandez-Corbaton, M. Juan, X. Vidal, and G. Molina-Terriza, Duality symmetry and Kerker conditions, Opt. Lett. **38**, 1857 (2013).

[36] J. Lasa-Alonso, J. Olmos-Trigo, A. García-Etxarri, and G. Molina-Terriza, Correlations between helicity and optical losses within general electromagnetic scattering theory, Mater. Adv. **3**, 4179 (2022).

[37] E. D. Palik, *Handbook of Optical Constants of Solids* (Academic Press, 1998), Vol 3.

[38] X. Zambrana-Puyalto, X. Vidal, and G. Molina-Terriza, Excitation of single multipolar modes with engineered cylindrically symmetric fields, Opt. Express **20**, 24536 (2012).

[39] C. Bohren and D. Huffman, *Absorption and Scattering of Light by Small Particles* (Wiley, 1983).

[40] R. Rangarajan, M. Goggin, and P. Kwiat, Optimizing type-I polarization-entangled photons, Opt. Express **17**, 18920 (2009).

[41] A. E. Siegman, *Lasers* (University Science Books, 1986).

[42] E. W. Weisstein, Associated Laguerre polynomial, https://mathworld.wolfram.com/.

[43] N. Tischler, X. Zambrana-Puyalto, and G. Molina-Terriza, The role of angular momentum in the construction of electromagnetic multipolar fields, Eur. J. Phys. **33**, 1099 (2012).

[44] M. Rose, Elementary theory of angular momentum, *Structure of Matter Series* (Wiley, 1957).

[45] L. Novotny and B. Hecht, *Principles of Nano-optics* (Cambridge University Press, 2012).

[46] Á. Nodar, R. Esteban, C. Maciel-Escudero, J. Lasa-Alonso, J. Aizpurua, and G. Molina-Terriza, Research data supporting "Preservation and destruction of the purity of two-photon states in the interaction with a classical nanoscatterer" [Data set] (2026), DIGITAL.CSIC, http://doi.org/10.20350/DIGITALCSIC/17893.